Self-Grown Ni(OH)$_2$ Layer on Bimodal Nanoporous AuNi Alloys for Enhanced Electrocatalytic Activity and Stability

Gao-Feng Han, Bei-Bei Xiao, Xing-You Lang,* Zi Wen, Yong-Fu Zhu, Ming Zhao, Jian-Chen Li, and Qing Jiang*

Key Laboratory of Automobile Materials, Ministry of Education, and School of Materials Science and Engineering, Jilin University, Changchun 130022, China

S *Supporting Information*

ABSTRACT: Au nanostructures as catalysts toward electro-oxidation of small molecules generally suffer from ultralow surface adsorption capability and stability. Here, we report Ni(OH)$_2$ layer decorated nanoporous (NP) AuNi alloys with a three-dimensional and bimodal porous architecture, which are facilely fabricated by a combination of chemical dealloying and in situ surface segregation, for the enhanced electrocatalytic performance in biosensors. As a result of the self-grown Ni(OH)$_2$ on the AuNi alloys with a coherent interface, which not only enhances adsorption energy of Au and electron transfer of AuNi/Ni(OH)$_2$ but also prohibits the surface diffusion of Au atoms, the NP composites are enlisted to exhibit significant enhancement in both electrocatalytic activity and stability toward glucose electrooxidation. The highly reliable glucose biosensing with exceptional reproducibility and selectivity as well as quick response makes it a promising candidate as electrode materials for the application in nonenzymatic glucose biosensors.

KEYWORDS: *nanoporous gold, nickel hydrate, biosensor, electrooxidation*
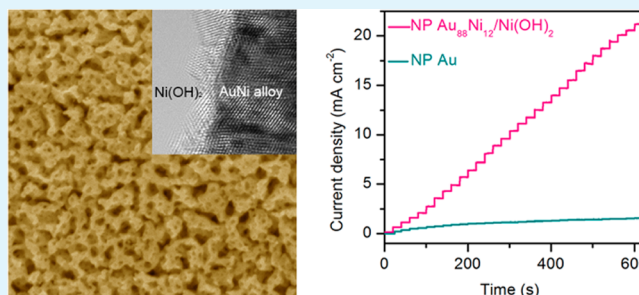
INTRODUCTION

Nanoporous (NP) metals, which possess fascinating physicochemical properties dramatically different from their bulk counterparts, have attracted considerable attention for many important applications, such as catalysis,[1,2] sensing,[3,4] actuation,[5] as well as energy storage and conversion.[6−9] NP metals can be made by chemically or electrochemically dealloying less-noble elements from precursor alloys, during which a three-dimensional (3D) and bicontinuous sponge structure of more-noble metal or alloy is produced with quasi-periodic metal ligaments and nanopore channels. The unique architecture enables NP metals to exhibit electrical conductivity comparable to the bulk value[10] and trap effectively more molecules for enhanced electrocatalysis.[11−14] By making use of these two properties, recently, NP Au is of special interest as one of model electrode materials and electrocatalysts toward the electrooxidation of small molecules in alkaline solution because of its exceptional resistance to the poisoning or inhibiting effect due to the adsorption of CO, which is a common byproduct of electrooxidation reactions.[15−18] Although Au generally suffers from a low surface adsorption capability, the high electrocatalytic activity of NP Au is demonstrated to result from the high-density steps and kinks on the geometrical surface,[19] which are thermodynamically instable.[20] This inevitably gives rise to the occurrence of a coarsening phenomenon that is usually observed on NP Au during potential cycling via fast surface diffusion, dramatically reducing its electrocatalytic

activity and long-term service life.[15,21] To circumvent these limitations, there have been a few approaches to be proposed for improving the performance of NP Au. These include alloying[22] and decorating in the bulk or on the surface of NP Au with noble metals with a low diffusion coefficient,[23,24] typically Pt[22−24] and Pd,[2] wherein small amounts of solute atoms segregate and accumulate on the surface, particularly at kink and step-edge sites, significantly improving both the nanostructural stability and the electrocatalytic activity of NP Au-based hybrids.[2,22−24] However, non-noble transition metals have attracted less attention, although they are expected to play a similar role in improving the performance of NP Au in electrocatalysis with much less cost. This is because they dissolve in an acid environment.[25−27] In the perspective that transition-metal oxides or hydroxides are stable in alkaline conditions, we make full use of surface segregation of transition metals and self-grown of their oxides or hydroxides on NP Au to ameliorate hydroxyl adsorption capability and thus electrocatalysis of Au.[28,29]

In this study, we report novel self-supported NP AuNi alloys that are decorated with a Ni(OH)$_2$ layer on their internal surface [NP AuNi/Ni(OH)$_2$] by a facile self-grown method in an electrochemical treatment, where surface segregation of Ni
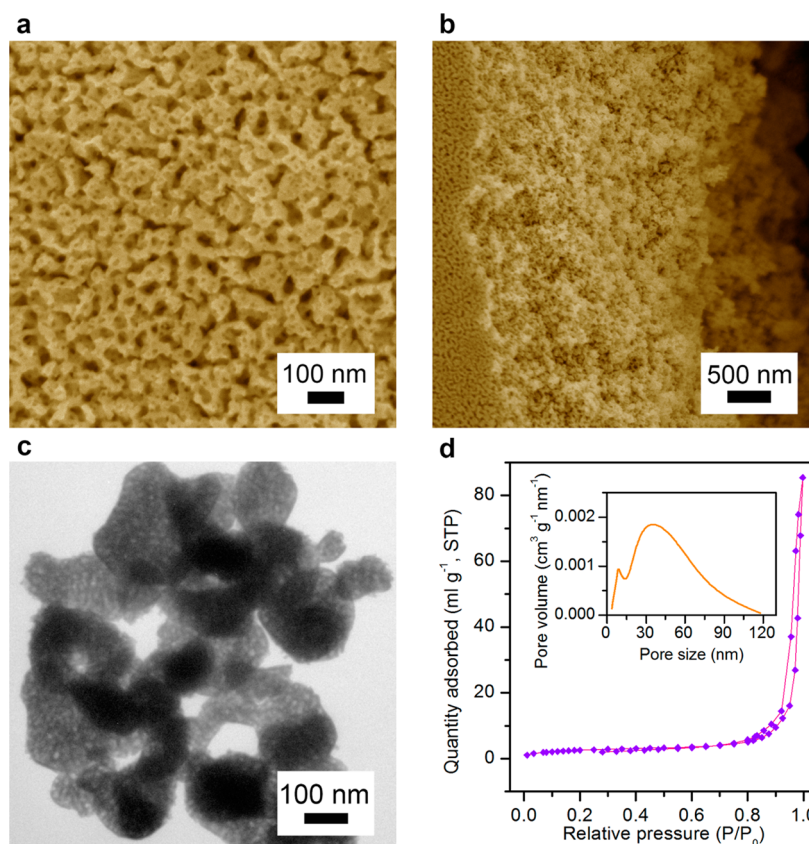
Figure 1. Microstructure characterization of as-dealloyed NP $Au_{88}Ni_{12}$. (a) Top-view and (b) cross-sectional SEM images of as-dealloyed NP $Au_{88}Ni_{12}$ ribbons with a bimodal nanoporosity consisting of small and large pores. (c) Typical TEM image of NP $Au_{88}Ni_{12}$. (d) Nitrogen adsorption−desorption isotherm of NP $Au_{88}Ni_{12}$ ribbon at 77 K. Inset: Pore size distributions of NP $Au_{88}Ni_{12}$ ribbon.

atoms takes place and then surface Ni atoms react in alkaline. The NP $AuNi/Ni(OH)_2$ hybrid electrodes exhibit exceptional electrocatalytic activity and stability toward electrooxidation of glucose for biosensors, showing promising application in glucose biosensors. The enhancement of electrocatalytic performance results from the unique hybrid architecture, in which the decoration of a small amount of $Ni(OH)_2$ not only enhances the adsorption capability of the NP Au but also blocks the surface diffusion of Au atoms and thus improves the stability of the porous structure. Furthermore, the $AuNi/Ni(OH)_2$ coherent interface decreases the contact resistance and facilitates the electron transfer between Au and $Ni(OH)_2$, offering the fast response to glucose.

■ EXPERIMENTAL METHODS

Fabrication of NP AuNi Alloys, NP AuNi/(OH)$_2$ Composites, and NP Au. The alloy of the $Au_{11}Ni_{10}Al_{79}$ (at. %) precursor was made from elemental Al (purity, 99.95 wt %), Au (purity, 99.99 wt %), and Ni (purity, 99.9 wt %) by arc melting in vacuum. Using a melt-spinning method, $Au_{11}Ni_{10}Al_{79}$ (at. %) ribbons with a cross section of ~20 μm × ~1 mm were prepared in a high-purity argon gas atmosphere from its ingot. The $Au_{11}Ni_{10}Al_{79}$ ribbons were chemically dealloyed in 1 M NaOH aqueous solution at room temperature for 40 min and at 90 °C for 60 min in sequence. The already etched ribbons were further treated in 0.25 M HNO_3 for tuning the composition of NP AuNi alloys. The NP $AuNi/Ni(OH)_2$ hybrid electrodes were fabricated by an in situ self-grown method, in which a potential cycling was performed in the potential window of −0.8 to 0.5 V at a scan rate of 50 mV s^{-1} in KOH electrolyte. The free-standing NP Au sheet with a thickness of ~20 μm was synthesized by chemically dealloying $Ag_{65}Au_{35}$ (at. %) in a 70% HNO_3 solution for 24 h at room

temperature. The selected longer dealloying time is to void any contaminants of Ag. The residual acid in NP specimens was removed by water rinsing for more than six times.

Characterization. The microstructure and chemical composition of the specimens were characterized using a field-emission scanning electron microscope (SEM, JEOL JSM-6700, 15 keV) equipped with an Oxford INCA x-sight energy-dispersive X-ray spectrometer (EDS) and a field-emission transmission electron microscope (TEM, JEOL JEM-2100F, 200 keV). X-ray photoelectron spectroscopy (XPS) characterization was performed on a Thermo ECSALAB 250 with an Al anode. The nitrogen adsorption and pore size distribution measurements were carried out using a Micromeritics ASAP 2020M surface area and porosity analyzer.

Electrochemical Measurement. All cyclic voltammetry (CV) and amperometric experiments were performed in a three-electrode setup, which employed NP Au, NP $Au_{52}Ni_{48}$, NP $Au_{88}Ni_{12}$, and NP $AuNi/Ni(OH)_2$ as the working electrodes and a Pt foil and a Ag/AgCl as the counter electrode and the reference electrode, respectively, in the 0.5 M KOH electrolyte bubbled by nitrogen gas for 30 min. The CV curves were collected in the aqueous electrolyte with and without 30 mM glucose. The amperometric responses of electrodes to glucose with a concentration of 1 mM were recorded under steady-state condition at a potential of 0.16 V (vs Ag/AgCl). To investigate the catalytic activity, the current was normalized by the electrochemical active surface area (ECSA), which was calculated in terms of the reduction peak of gold.

Calculation Method. All calculations are performed within the DFT framework as implemented in the CASTEP code. The generalized gradient approximation with the Perdew−Burke−Ernzerhof (PBE) functional is employed to describe exchange and correlation effects.[30] For improving the calculation efficiency, the ultrasoft pseudopetentails core treat method is implemented.[31] A smearing of 0.1 eV to the orbital occupation is applied to achieve
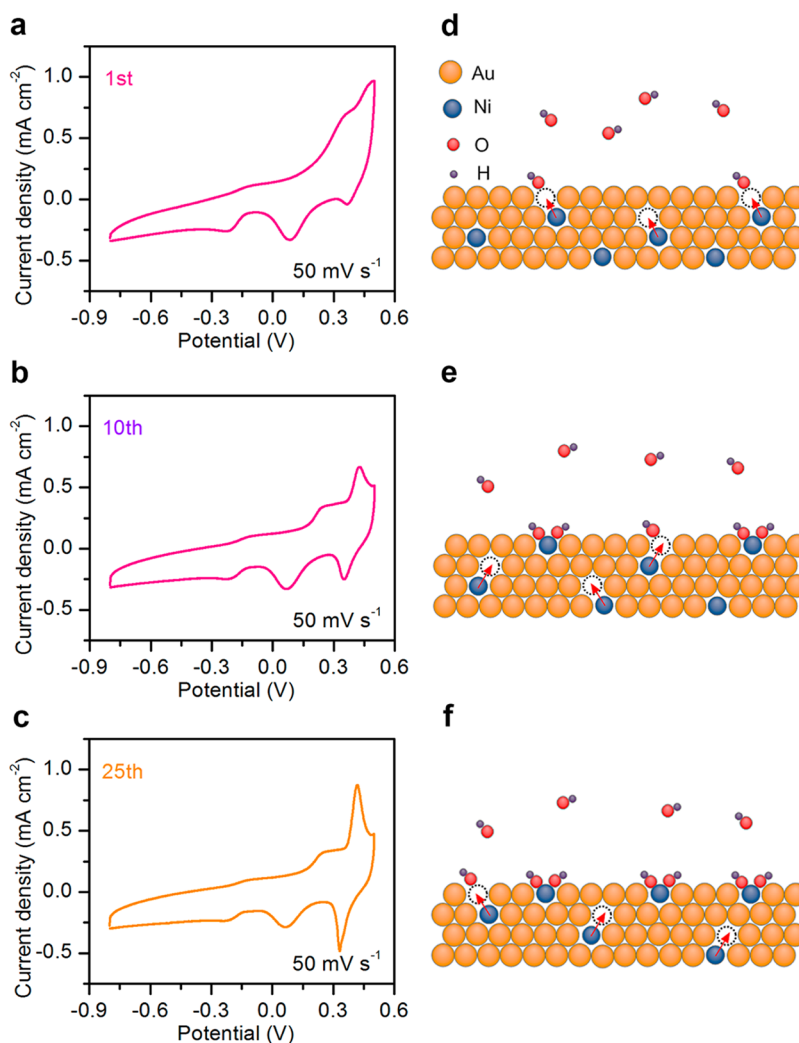
Figure 2. CV curves of NP $Au_{88}Ni_{12}$ at (a) the 1st, (b) the 10th, and (c) the 25th cycles in 0.5 M KOH aqueous solution at a scan rate of 50 mV s^{-1}. (d, e, f) Schematics to illustrate the Ni atom diffusion and the formation of $Ni(OH)_2$ on the NP AuNi alloy surface in the electrochemical process of surface segregation.

accurate electronic convergence. Further details are available in the Supporting Information.

■ RESULTS AND DISCUSSION

The composition at the surface may deviate from that in the interior, not only depending on the heat of segregation and the surface mixing energy of a bimetallic alloy but also additionally relying on the chemical potential in the gas or aqueous phase because of the energy gain of the whole system with the strong component/adsorbate bonding.[32,33] As a consequence, the component that binds a certain adsorbate more strongly may become rich at the surface of the bimetallic alloy. In light of the distinct difference of adsorption energies for OH$^-$ on Au and Ni elements, we demonstrate this process to be one of useful and facile methods to fabricate NP AuNi/Ni(OH)$_2$ electrode materials with enhanced electrocatalytic performance. Here, NP AuNi alloys are first fabricated by chemically dealloying 20 μm thick $Au_{11}Ni_{10}Al_{79}$ (at. %) ternary alloy ribbons (Figure S1a; see the Supporting Information) that are produced by single-roller metal-spinning in vacuum from their ingot composed of a uniform α-Al metal and $AuAl_2Ni_x$ alloy intermixture (Figure S1b). There are no extra diffraction peaks for possible phases of Ni, suggesting the formation of the disordered single-phase

$AuAl_2Ni_x$ alloy.[34] The α-Al in the mixture is rapidly dissolved from the entire ribbons during the chemical dealloying in 1 M NaOH aqueous solution at room temperature. While in the already dealloyed $AuAl_2Ni_x$ alloy, the less noble Al component is fully selectively etched in 1 M NaOH at 90 °C (Figure S1c,d). The as-prepared NP $Au_{52}Ni_{48}$ alloy is further treated in 0.25 M HNO$_3$ for 90 min to tune the Ni component in NP AuNi alloys. Figure 1a,b shows typical top-view and cross-sectional SEM images of the as-dealloyed NP AuNi alloy with an atomic rate of 88:12 (NP $Au_{88}Ni_{12}$) (Figure S2, Supporting Information) and a bimodal NP architecture, which consists of quasi-periodic $Au_{88}Ni_{12}$ ligaments and nanopore channels with characteristic lengths of ~5 and ~45 nm (Figure S3, Supporting Information). The unique bimodal NP structure is further verified by TEM (Figure 1c) and N$_2$ sorption analysis (Figure 1d). As shown in the adsorption isotherm of the NP $Au_{88}Ni_{12}$ alloy, there are two hysteresis loops at high and low relative pressures (Figure 1d). The pore distribution curve indicates that the sizes of small and large pores are ~8 and ~37 nm (inset of Figure 1d), approximately consistent with the image analysis (Figure S3).[35]

To decorate the Ni(OH)$_2$ layer on the internal surface of the NP skeleton, the as-dealloyed NP $Au_{88}Ni_{12}$ is subject to an
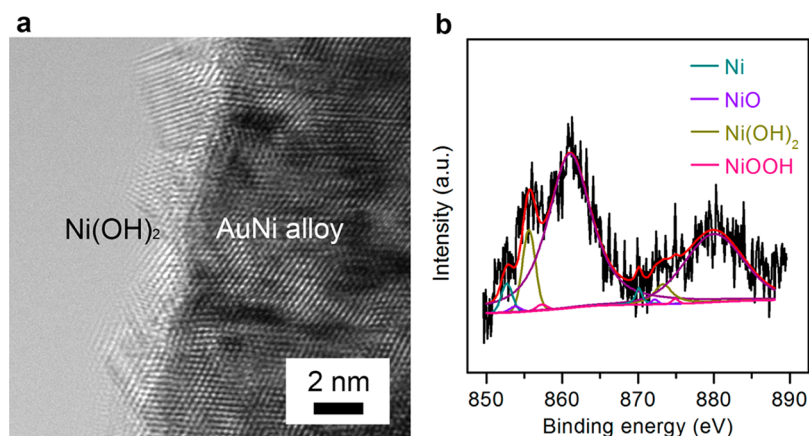
Figure 3. (a) HRTEM image of NP $Au_{88}Ni_{12}/Ni(OH)_2$ interface structure. (b) High-resolution XPS spectrum of Ni 2p on NP $Au_{88}Ni_{12}/Ni(OH)_2$ surface.
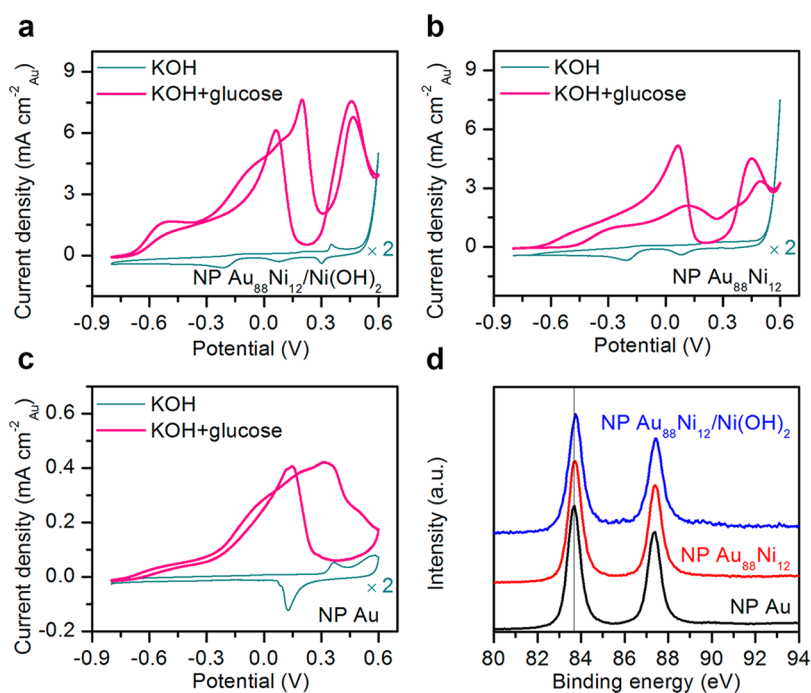
Figure 4. CV curves of (a) NP $Au_{88}Ni_{12}/Ni(OH)_2$, (b) NP $Au_{88}Ni_{12}$, and (c) NP Au in 0.5 M N_2-saturated KOH solution with and without 30 mM glucose at a scan rate of 10 mV s^{-1}. (d) High-resolution XPS spectra of Au 4f for NP $Au_{88}Ni_{12}/Ni(OH)_2$, NP $Au_{88}Ni_{12}$, and NP Au, respectively.

electrochemical treatment in an alkaline electrolyte, where the surface segregation occurs during the potential cycling as a result of fast surface diffusion of Au atoms and the strong bonding between Ni and OH$^-$. This process is monitored using the surface-sensitive cyclic voltammetry.[32] Figure 2a shows the first CV curve of the untreated NP $Au_{88}Ni_{12}$ in a N_2-purged electrolyte at a scan rate of 50 mV s^{-1}, where no redox peaks of Ni can be observed. This indicates that there is not any Ni atoms on the surface of the as-dealloyed NP $Au_{88}Ni_{12}$. During the potential cycling, the surface Au atoms on NP $Au_{88}Ni_{12}$ move via fast surface diffusion and the buried Ni atoms are exposed to the alkaline electrolyte for the production of Ni(OH)$_2$ on the surface (Figure 2d). Therefore, in the subsequent cycles, the redox peaks of Ni are identified legibly at the potentials of 0.42 V for oxidation and 0.33 V for reduction, implying the occurrence of surface segregation of Ni from the inner of AuNi alloy ligaments (Figure 2b). The subskin Ni atoms are further attracted to the surface of

ligaments via vacancy exchange because of their strong affinity for OH$^-$ (Figure 2e). This gives rise to the increase of the current density of Ni redox peaks with the increasing cycle number (Figure 2c) until the heat of segregation and the surface mixing energy reach a balance at the surface after 25 cycles (Figure 2f).[32,33] The occurrence of surface segregation in $Au_{88}Ni_{12}$ results from the different oxophilicity between Au and Ni components. This is verified by density functional theory (DFT) investigation (Figure S4, Supporting Information). For the AuNi alloy with a bare surface, the $Au_{88}Ni_{12}$ ligament covered with a pure Au skin is thermodynamically more stable because the surface energy of Au is much lower than that of Ni[36] and the segregation energy (E_{seg}) is 0.31 eV. While in the presence of OH$^-$, the AuNi mixture skin is preferred with E_{seg} ≈ −0.81 eV as a result of the stronger interaction between Ni and OH*. Figure 3a shows the high-resolution TEM image of the NP $Au_{88}Ni_{12}/Ni(OH)_2$ composite, where the contrast difference between $Au_{88}Ni_{12}$ and the Ni(OH)$_2$ layer can be
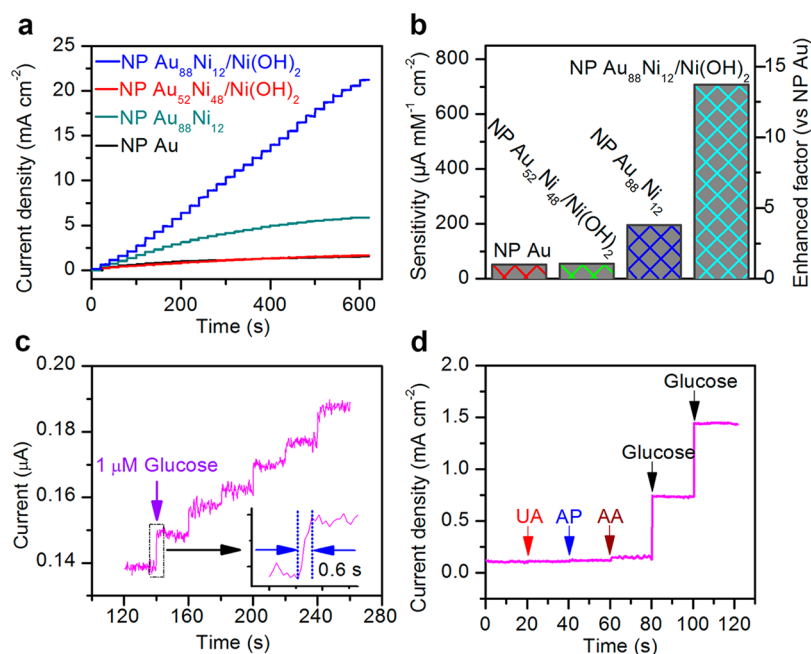
Figure 5. (a) Chronoamperometry curves for NP Au$_{88}$Ni$_{12}$/Ni(OH)$_2$, NP Au$_{52}$Ni$_{48}$/Ni(OH)$_2$, NP Au$_{88}$Ni$_{12}$, and NP Au electrodes for the successive addition of glucose with a concentration of 1 mM at a potential of 0.16 V (vs Ag/AgCl) in 0.5 M N$_2$-saturated KOH solution. (b) Comparison of the sensitivities of NP Au$_{88}$Ni$_{12}$/Ni(OH)$_2$, NP Au$_{52}$Ni$_{48}$/Ni(OH)$_2$, NP Au$_{88}$Ni$_{12}$, and NP Au for a glucose concentration of 1 mM. (c) Amperometric response to glucose with the low limit concentrations of 1 μM ($S/N = 3$). Inset: The fast response of 0.6 s to the glucose. All are tested. (d) Amperometric response to the successive addition of interfering compounds such as 0.02 mM uric acid (UA), 0.1 mM acetamidophenol (AP), 0.1 mM ascorbic acid (AA), and as well as 1 mM glucose at a potential of 0.16 V.

identified. The crystalline Ni(OH)$_2$ layer epitaxially grows on the AuNi ligaments by end-bonded contact, offering excellent electrical conductivity and stable interface structure.[3] The chemical state of Ni on the NP Au$_{88}$Ni$_{12}$/Ni(OH)$_2$ is further verified by XPS characterization. As shown in Figure 3b, the Ni 2p$_{3/2}$ XPS peaks at the binding energies of 852.7, 853.8, 855.6, and 857.3 eV correspond to metallic Ni, NiO, Ni(OH)$_2$, and NiOOH, respectively, after taking account of the shake-up peaks.[37,38] In addition to negligible NiO and NiOOH, there are primarily Ni(OH)$_2$ and metallic Ni with the atomic ratios of 70% and 21%, respectively. The latter is attributed to the nonsegregation Ni in the AuNi alloy.

To demonstrate the electrocatalytic activity toward electrooxidation of small molecules for the NP Au$_{88}$Ni$_{12}$/Ni(OH)$_2$ hybrid electrode material, glucose is employed as a probe molecule. All electrochemical measurements are carried out using a typical three-electrode configuration with a Pt counter electrode and a Ag/AgCl reference electrode at room temperature. Figure 4a shows the representative CV curve of NP Au$_{88}$Ni$_{12}$/Ni(OH)$_2$ in a N$_2$-saturated 0.5 M KOH electrolyte with glucose at a scan rate of 10 mV s^{-1}, in distinct contrast with its blank voltammetry (without glucose) due to the glucose oxidation. In the glucose-free alkaline solution, the CV response of NP Au$_{88}$Ni$_{12}$/Ni(OH)$_2$ illustrates the electrochemical features of both Au and the Ni(OH)$_2$ (Figure 4a).[17,18,39] For comparison, the typical CV curves of the NP Au$_{88}$Ni$_{12}$ and pure NP Au in the same electrolytes are shown in Figure 4b,c. Owing to the decoration of Ni(OH)$_2$, the CV of the NP Au$_{88}$Ni$_{12}$/Ni(OH)$_2$ electrode shows a much more negative onset potential of OH* adsorption and higher anodic current density in the electrolyte of KOH and glucose mixture compared with these in the NP Au$_{88}$Ni$_{12}$ and pure NP Au. Furthermore, the peak currents of glucose electrooxidation at

the corresponding Au and Ni(OH)$_2$ of NP Au$_{88}$Ni$_{12}$/Ni(OH)$_2$ increase linearly as a function of the square root of the scan rate (Figure S5a,b, Supporting Information),[40,41] which is the same as that of bare NP Au (Figure S5c,d). It implies that the NP Au$_{88}$Ni$_{12}$/Ni(OH)$_2$ exhibits higher electrocatalytic activity toward glucose electrooxidation than the NP Au$_{88}$Ni$_{12}$ and Au in a wide potential due to the decoration of the Ni(OH)$_2$ layer.[41] A positive shift of 0.05 eV of the Au 4f$_{7/2}$ XPS peak is observed on the NP Au$_{88}$Ni$_{12}$/Ni(OH)$_2$ in comparison with the NP Au (Figure 4d), accounting for the synergistic electrocatalysis of Au and Ni(OH)$_2$ toward glucose oxidation.[37,38,42]

This enhancement of activity toward glucose electrooxidation enlists the NP Au$_{88}$Ni$_{12}$/Ni(OH)$_2$ electrode to exhibit outstanding performance of glucose biosensing, which is evaluated by amperometric measurements at a low potential of 0.16 V. Figure 5a shows a typical current−time curve of the NP Au$_{88}$Ni$_{12}$/Ni(OH)$_2$ electrode with the successive addition of 1 mM glucose. The amperometric response of NP Au$_{88}$Ni$_{12}$/Ni(OH)$_2$ displays a perfect and stable step curve with a remarkably enhanced current density in comparison with these of the NP Au$_{88}$Ni$_{12}$ and NP Au, which are also included in this plot for comparison. Furthermore, the NP Au$_{88}$Ni$_{12}$/Ni(OH)$_2$ always remains a linear response in the range of the glucose addition up to the concentration of 30 mM, much higher than these for the NP Au$_{88}$Ni$_{12}$ (∼20 mM) and NP Au (∼10 mM), as shown in Figure S6 (Supporting Information) for their calibration curves. In the whole linear range, the sensitivity of NP Au$_{88}$Ni$_{12}$/Ni(OH)$_2$ reaches 707 μA mM^{-1} cm^{-2}, 3- and 13-fold higher than these of NP Au$_{88}$Ni$_{12}$ (∼196 μA mM^{-1} cm^{-2}) and NP Au (∼51 μA mM^{-1} cm^{-2}), respectively (Figure 5b). Such a high sensitivity offers the NP Au$_{88}$Ni$_{12}$/Ni(OH)$_2$ electrode a detection limit as low as 1 μM (Figure 5c) and a response time no more than 0.6 s to reach steady-state current
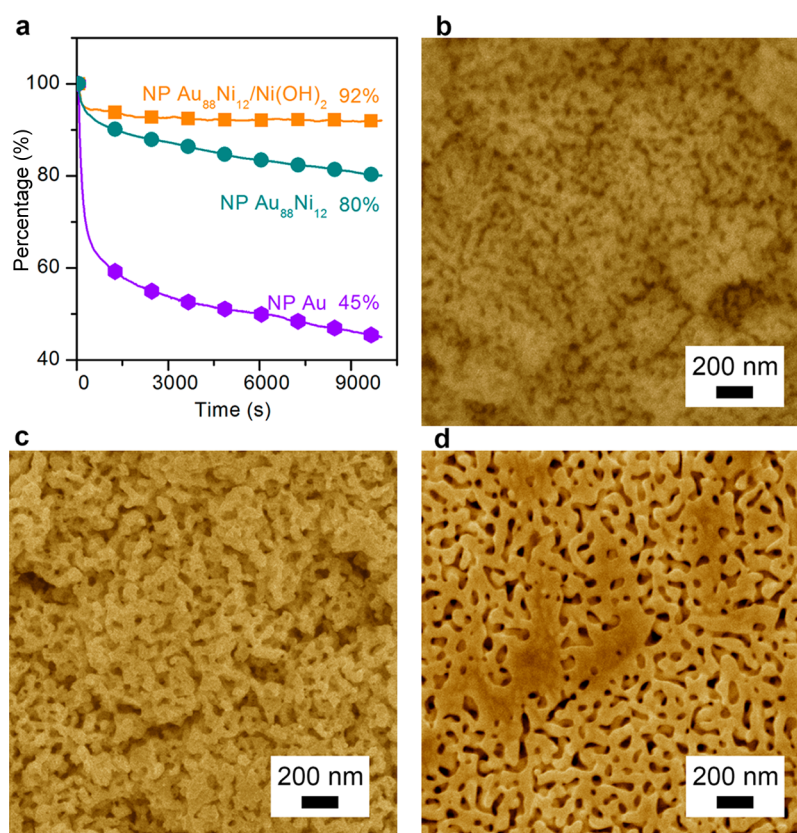
Figure 6. (a) Electrochemical stability for NP $Au_{88}Ni_{12}/Ni(OH)_2$, NP $Au_{88}Ni_{12}$, and NP Au over 10 000 s at 0.16 V. Typical SEM images of (b) NP $Au_{88}Ni_{12}/Ni(OH)_2$, (c) NP $Au_{88}Ni_{12}$, and (d) NP Au after stability test.

(inset of Figure 5c), much faster than 2 s for a nanometal-decorated graphite nanoplatelet,[43] and 6 s for GOx-CNT networks.[44] Moreover, the NP $Au_{88}Ni_{12}/Ni(OH)_2$ electrode provides a prominent selectivity for glucose detection at the low potential of 0.16 V, which minimizes the responses of common interference species such as uric acid (UA), acetamidophenol (AP), and ascorbic acid (AA) in physiological levels (Figure 5d). Additions of 0.02 mM UA, 0.1 mM AP, or 0.1 mM AA to a 1 mM glucose solution result in only about 0.5−4% increases in the current density and do not interfere with the glucose detection even without the permselective coatings. These predominant properties enlist the self-grown NP $Au_{88}Ni_{12}/Ni(OH)_2$ electrode to exhibit high reliability for analyzing the glucose level.

The high-performance glucose biosensing of NP $Au_{88}Ni_{12}/Ni(OH)_2$ results from the high electrocatalysis toward glucose oxidation due to the enhanced electron transfer between the NP AuNi skeleton and the $Ni(OH)_2$ layer, wherein the former offers the ultrahigh conductivity and facilitates analyte transport in the electrode system, and the latter improves the adsorption capability of Au. It should be noted that, as a result of the decoration of the $Ni(OH)_2$ layer on the surface of the AuNi alloy, the electrocatalytic activities of NP $AuNi/Ni(OH)_2$ electrodes are remarkably influenced by the Ni components (Figure 5 and Figure S7, Supporting Information). As the Ni component increases from 0 to 12%, the electrocatalytic activity starts to increase and reaches its maximum at a component of 12%. While the Ni component in the NP AuNi alloy continues to increase, the activity begins to reduce evidently (Figure S7b). For instance, for NP $Au_{52}Ni_{48}$ that is achieved by just dealloying $Au_{11}Ni_{10}Al_{79}$ (at. %) ribbons in KOH aqueous solution (Figure

S1c,d), there will be an excessive amount of $Ni(OH)_2$ to be produced in the potential cycling because of the surface segregation of Ni atoms and the reaction with alkaline [NP $Au_{52}Ni_{48}/Ni(OH)_2$]. This gives rise to a too high adsorption energy of glucose to block the electrooxidation on the surface of NP $Au_{52}Ni_{48}/Ni(OH)_2$, enabling the low-performance of glucose biosensing, as shown in Figure 5a,b, where the sensitivity ($\sim$54 μA mM^{-1} cm^{-2}) is just a little higher than that of NP Au.

Figure 6a compares the electrochemical stabilities of the NP $Au_{88}Ni_{12}/Ni(OH)_2$, NP $Au_{88}Ni_{12}$, and NP Au electrodes, which are investigated by the chronoamperometric method at an applied potential of 0.16 V in a N_2-saturated mixture of 0.5 M KOH and 30 mM glucose. In spite of the slow decrease of current at the beginning of the measurement, the current of NP $Au_{88}Ni_{12}/Ni(OH)_2$ remains steady over the long-term operation. After the 10 000 s durability test, the NP $Au_{88}Ni_{12}/Ni(OH)_2$ electrode retains $\sim$92% of the initial current, whereas the NP $Au_{88}Ni_{12}$ and NP Au lose 20% and 55%, respectively (Figure 6a). The prominent stability of NP $Au_{88}Ni_{12}/Ni(OH)_2$ is attributed to the Ni hydroxide and Ni atom that pin the surface Au atoms, particularly sitting kink and step-edge sites, similar to the observation that the addition of low-surface-diffusion Pt can stabilize the microstructure of NP Au.[22,45] As shown in Figure 6b,c, the NP structure of NP $Au_{88}Ni_{12}/Ni(OH)_2$ and NP $Au_{88}Ni_{12}$ does not change much compared with the initial SEM images (Figure S8a, Supporting Information). In distinct contrast, severe coarsening takes place on NP Au due to the fast surface diffusion of Au atoms,[15,20] which gives rise to the poor electrochemical durability of NP Au during the long time test (Figure 6d and Figure S8b).

CONCLUSION

We have demonstrated a facile self-grown method to fabricate NP $Au_{88}Ni_{12}/Ni(OH)_2$ hybrids with a 3D bimodal nanoporous architecture by making full use of the surface segregation of transition metals and the sequent in situ formation of hydroxides. The in situ method produces the inherent coherent $Au_{88}Ni_{12}/Ni(OH)_2$ interface, enlisting NP $Au_{88}Ni_{12}/Ni(OH)_2$ to exhibit outstanding performance of electrocatalysis toward glucose oxidization and thus the glucose biosensing. The exceptionally high electrocatalytic activity and durability of NP $Au_{88}Ni_{12}/Ni(OH)_2$ results from the unique architecture, in which the NP AuNi skeleton offers high conductivity and traps more analyte molecules in its channels while the $Ni(OH)_2$ layer enhances the adsorption capability and blocks the fast surface diffusion of surface Au atoms. This approach can be extended to other alloy systems for improving their electrochemical performance by decorating transition-metal hydroxides on the surface.

ASSOCIATED CONTENT

Ⓢ Supporting Information

Computer calculation method, EDS spectra and XRD patterns, computer calculation atom structures, CV curves and calibration current curves, and SEM images. This material is available free of charge via the Internet at http://pubs.acs.org.

AUTHOR INFORMATION

Corresponding Authors
*E-mail: xylang@jlu.edu.cn (X.-Y.L.).
*E-mail: jiangq@jlu.edu.cn (Q.J.).
Notes
The authors declare no competing financial interest.

ACKNOWLEDGMENTS

REFERENCES

(1) Wichmann, A.; Wittstock, A.; Frank, K.; Biener, M. M.; Neumann, B.; Mädler, L.; Biener, J.; Rosenauer, A.; Bäumer, M. Maximizing Activity and Stability by Turning Gold Catalysis Upside Down: Oxide Particles on Nanoporous Gold. *ChemCatChem* **2013**, *5*, 2037−2043.

(2) Lang, X. Y.; Guo, H.; Chen, L. Y.; Kudo, A.; Yu, J. S.; Zhang, W.; Inoue, A.; Chen, M. W. Novel Nanoporous Au-Pd Alloy with High Catalytic Activity and Excellent Electrochemical Stability. *J. Phys. Chem. C* **2010**, *114*, 2600−2603.

(3) Lang, X. Y.; Fu, H. Y.; Hou, C.; Han, G. F.; Yang, P.; Liu, Y. B.; Jiang, Q. Nanoporous Gold Supported Cobalt Oxide Microelectrodes as High-Performance Electrochemical Biosensors. *Nat. Commun.* **2013**, *4*, 2169.

(4) Huang, J. F. Facile Preparation of an Ultrathin Nickel Film Coated Nanoporous Gold Electrode with the Unique Catalytic Activity to Oxidation of Glucose. *Chem. Commun.* **2009**, 1270−1272.

(5) Biener, M. M.; Biener, J.; Wichmann, A.; Wittstock, A.; Baumann, T. F.; Bäumer, M.; Hamza, A. V. ALD Functionalized Nanoporous Gold: Thermal Stability, Mechanical Properties, and Catalytic Activity. *Nano Lett.* **2011**, *11*, 3085−3090.

(6) Kang, J. L.; Hirata, A.; Qiu, H. J.; Chen, L. Y.; Ge, X. B.; Fujita, T.; Chen, M. W. Self-Grown Oxy-Hydroxide@ Nanoporous Metal Electrode for High-Performance Supercapacitors. *Adv. Mater.* **2014**, *26*, 269−272.

(7) Lang, X. Y.; Hirata, A.; Fujita, T.; Chen, M. W. Nanoporous Metal/Oxide Hybrid Electrodes for Electrochemical Supercapacitors. *Nat. Nanotechnol.* **2011**, *6*, 232−236.

(8) Lang, X. Y.; Hirata, A.; Fujita, T.; Chen, M. W. Three-Dimensional Hierarchical Nanoporosity for Ultrahigh Power and Excellent Cyclability of Electrochemical Pseudocapacitors. *Adv. Energy Mater.* **2014**, *4*, 1301809.

(9) Hou, C.; Lang, X. Y.; Han, G. F.; Li, Y. Q.; Zhao, L.; Wen, Z.; Zhu, Y. F.; Zhao, M.; Li, J. C.; Lian, J. S.; Jiang, Q. Integrated Solid/Nanoporous Copper/Oxide Hybrid Bulk Electrodes for High-Performance Lithium-Ion Batteries. *Sci. Rep.* **2013**, *3*, 2878.

(10) Fujita, T.; Okada, H.; Koyama, K.; Watanabe, K.; Maekawa, S.; Chen, M. W. Unusually Small Electrical Resistance of Three-Dimensional Nanoporous Gold in External Magnetic Fields. *Phys. Rev. Lett.* **2008**, *101*, 166601.

(11) Zhan, B. B.; Liu, C. B.; Chen, H. P.; Shi, H. X.; Wang, L. H.; Chen, P.; Huang, W.; Dong, X. C. Free-Standing Electrochemical Electrode Based on $Ni(OH)_2$/3D Graphene Foam for Nonenzymatic Glucose Detection. *Nanoscale* **2014**, *6*, 7424−7429.

(12) Elvira, K. S.; Solvas, X. C.; Wootton, R. C. R.; DeMello, A. J. The Past, Present and Potential for Microfluidic Reactor Technology in Chemical Synthesis. *Nat. Chem.* **2013**, *5*, 905−915.

(13) Park, S. Y.; Kim, H. C.; Chung, T. D. Electrochemical Analysis Based on Nanoporous Structures. *Analyst* **2012**, *137*, 3891−3903.

(14) Ding, L. X.; Wang, A. L.; Li, G. R.; Liu, Z. Q.; Zhao, W. X.; Su, C. Y.; Tong, Y. X. Porous Pt-Ni-P Composite Nanotube Arrays: Highly Electroactive and Durable Catalysts for Methanol Electro-oxidation. *J. Am. Chem. Soc.* **2012**, *134*, 5730−5733.

(15) Zhang, J. T.; Liu, P. P.; Ma, H.; Ding, Y. Nanostructured Porous Gold for Methanol Electro-Oxidation. *J. Phys. Chem. C* **2007**, *111*, 10382−10388.

(16) Xu, C. X.; Su, J. X.; Xu, X. H.; Liu, P. P.; Zhao, H. J.; Tian, F.; Ding, Y. Low Temperature CO Oxidation over Unsupported Nanoporous Gold. *J. Am. Chem. Soc.* **2007**, *129*, 42−43.

(17) Seo, B.; Kim, J. W. Electrooxidation of Glucose at Nanoporous Gold Surfaces: Structure Dependent Electrocatalysis and Its Application to Amperometric Detection. *Electroanalysis* **2010**, *22*, 939−945.

(18) Chen, L. Y.; Lang, X. Y.; Fujita, T.; Chen, M. W. Nanoporous Gold for Enzyme-Free Electrochemical Glucose Sensors. *Scr. Mater.* **2011**, *65*, 17−20.

(19) Fujita, T.; Guan, P. F.; McKenna, K.; Lang, X. Y.; Hirata, A.; Zhang, L.; Tokunaga, T.; Arai, S.; Yamamoto, Y. Y.; Tanaka, N.; Ishikawa, Y.; Asao, N.; Erlebacher, J. D.; Chen, M. W. Atomic Origins of the High Catalytic Activity of Nanoporous Gold. *Nat. Mater.* **2012**, *11*, 775−780.

(20) Fujita, T.; Tokunaga, T.; Zhang, L.; Li, D. W.; Chen, L. Y.; Arai, S.; Yamamoto, Y.; Hirata, A.; Tanaka, N.; Ding, Y.; Chen, M. W. Atomic Observation of Catalysis-Induced Nanopore Coarsening of Nanoporous Gold. *Nano Lett.* **2014**, *14*, 1172−1177.

(21) Erlebacher, J. D.; Aziz, M. J.; Karma, A.; Dimitrov, N.; Sieradzki, K. Evolution of Nanoporosity in Dealloying. *Nature* **2001**, *410*, 450−453.

(22) Snyder, J.; Asanithi, P.; Dalton, A. B.; Erlebacher, J. D. Stabilized Nanoporous Metals by Dealloying Ternary Alloy Precursors. *Adv. Mater.* **2008**, *20*, 4883−4886.

(23) Wang, R. Y.; Wang, C.; Cai, W. B.; Ding, Y. Ultralow-Platinum-Loading High-Performance Nanoporous Electrocatalysts with Nano-engineered Surface Structures. *Adv. Mater.* **2010**, *22*, 1845−1848.

(24) Wang, R. Y.; Liu, J. G.; Liu, P.; Bi, X. X.; Yan, X. L.; Wang, W. X.; Ge, X. B.; Chen, M. W.; Ding, Y. Dispersing Pt Atoms onto Nanoporous Gold for High Performance Direct Formic Acid Fuel Cells. *Chem. Sci.* **2014**, *5*, 403−409.

(25) Cui, C. H.; Ahmadi, M.; Behafarid, F.; Gan, L.; Neumann, M.; Heggen, M.; Cuenya, B. R.; Strasser, P. Shape-Selected Bimetallic

Nanoparticle Electrocatalysts: Evolution of Their Atomic-Scale Structure, Chemical Composition, and Electrochemical Reactivity under Various Chemical Environments. *Faraday Discuss.* **2013**, *162*, 91−112.

(26) Tuaev, X.; Rudi, S.; Petkov, V.; Hoell, A.; Strasser, P. In Situ Study of Atomic Structure Transformations of Pt−Ni Nanoparticle Catalysts during Electrochemical Potential Cycling. *ACS Nano* **2013**, *7*, 5666−5674.

(27) Cui, C. H.; Gan, L.; Heggen, M.; Rudi, S.; Strasser, P. Compositional Segregation in Shaped Pt Alloy Nanoparticles and Their Structural Behaviour during Electrocatalysis. *Nat. Mater.* **2013**, *12*, 765−771.

(28) Molina, L.; Hammer, B. Active Role of Oxide Support during CO Oxidation at Au/MgO. *Phys. Rev. Lett.* **2003**, *90*, 206102.

(29) Liu, Z. P.; Gong, X. Q.; Kohanoff, J.; Sanchez, C.; Hu, P. Catalytic Role of Metal Oxides in Gold-Based Catalysts: A First Principles Study of CO Oxidation on TiO_2 Supported Au. *Phys. Rev. Lett.* **2003**, *91*, 266102.

(30) Perdew, J. P.; Burke, K.; Ernzerhof, M. Generalized Gradient Approximation Made Simple. *Phys. Rev. Lett.* **1996**, *77*, 3865−3868.

(31) Rappe, A. M.; Rabe, K. M.; Kaxiras, E.; Joannopoulos, J. D. Optimized Pseudopotentials. *Phys. Rev. B* **1990**, *41*, 1227−1230.

(32) Mayrhofer, K. J. J.; Juhart, V.; Hartl, K.; Hanzlik, M.; Arenz, M. Adsorbate-Induced Surface Segregation for Core-Shell Nanocatalysts. *Angew. Chem., Int. Ed.* **2009**, *48*, 3529−3531.

(33) Christensen, A.; Ruban, A.; Stoltze, P.; Jacobsen, K.; Skriver, H.; Nørskov, J. K.; Besenbacher, F. Phase Diagrams for Surface Alloys. *Phys. Rev. B* **1997**, *56*, 5822−5834.

(34) Wang, Y.; Xu, J. L.; Wu, B. Electrochemical Dealloying of $Al_2(Au,X)$ (X = Pt, Pd, PtPd, Ni, Co and NiCo) Alloys in NaCl Aqueous Solution. *Phys. Chem. Chem. Phys.* **2013**, *15*, 5499−5509.

(35) Song, T. T.; Gao, Y. L.; Zhang, Z. H.; Zhai, Q. J. Dealloying Behavior of Rapidly Solidified Al-Ag Alloys to Prepare Nanoporous Ag in Inorganic and Organic Acidic Media. *CrystEngComm* **2011**, *13*, 7058−7067.

(36) Jiang, Q.; Lu, H. M.; Zhao, M. Modelling of Surface Energies of Elemental Crystals. *J. Phys.: Condens. Matter* **2004**, *16*, 521−530.

(37) Park, K. W.; Choi, J. H.; Kwon, B. K.; Lee, S. A.; Sung, Y. E.; Ha, H. Y.; Hong, S. A.; Kim, H.; Wieckowski, A. Chemical and Electronic Effects of Ni in Pt/Ni and Pt/Ru/Ni Alloy Nanoparticles in Methanol Electrooxidation. *J. Phys. Chem. B* **2002**, *106*, 1869−1877.

(38) Yan, S. H.; Gao, L. Z.; Zhang, S. C.; Gao, L. L.; Zhang, W. K.; Li, Y. Z. Investigation of AuNi/C Anode Catalyst for Direct Methanol Fuel Cells. *Int. J. Hydrogen Energy* **2013**, *38*, 12838−12846.

(39) Lu, W.; Qin, X.; Asiri, A. M.; Al-Youbi, A. O.; Sun, X. Ni Foam: A Novel Three-Dimensional Porous Sensing Platform for Sensitive and Selective Nonenzymatic Glucose Detection. *Analyst* **2013**, *138*, 417−420.

(40) Walcarius, A. Mesoporous Materials and Electrochemistry. *Chem. Soc. Rev.* **2013**, *42*, 4098−4140.

(41) Li, S.; Zheng, Y. J.; Qin, G. W.; Ren, Y. P.; Pei, W. L.; Zuo, L. Enzyme-Free Amperometric Sensing of Hydrogen Peroxide and Glucose at a Hierarchical Cu_2O Modified Electrode. *Talanta* **2011**, *85*, 1260−1264.

(42) Yang, T.; Zhang, L. J.; Li, X.; Xia, D. G. Structural and Morphological Characterization of Gold-Nickel Electrocatalyst Synthesized by Taking Advantage of the AuNi Phase Separation Mechanism. *J. Alloys Compd.* **2010**, *492*, 83−87.

(43) Lu, J.; Do, I.; Drzal, L. T.; Worden, R. M.; Lee, I. Nanometal-Decorated Exfoliated Graphite Nanoplatelet Based Glucose Biosensors with High Sensitivity and Fast Response. *ACS Nano* **2008**, *2*, 1825−1832.

(44) Claussen, J. C.; Franklin, A. D.; Haque, A. U.; Porterfield, D. M.; Fisher, T. S. Electrochemical Biosensor of Nanocube-Augmented Carbon Nanotube Networks. *ACS Nano* **2009**, *3*, 37−44.

(45) Jin, H. J.; Wang, X. L.; Parida, S.; Wang, K.; Seo, M.; Weissmüller, J. Nanoporous Au-Pt Alloys as Large Strain Electrochemical Actuators. *Nano Lett.* **2010**, *10*, 187−194.